RSC Advances

PAPER

View Article Online
View Journal | View Issue

Cite this: *RSC Adv.*, 2024, **14**, 15664

Preparation and characterization of various PVPylated divalent metal-doped ferrite nanoparticles for magnetic hyperthermia†

Kheireddine El-Boubbou, *[a] O. M. Lemine, *[b] Saja Algessair,[b] Nawal Madkhali,[b] Basma Al-Najar,[c] Enas AlMatri,[a] Rizwan Ali [d] and Mohamed Henini[e]

There is an incessant demand to keep improving on the heating responses of polymeric magnetic nanoparticles (MNPs) under magnetic excitation, particularly in the pursuit for them to be utilized for clinical hyperthermia applications. Herein, we report the fabrication of a panel of PVP-capped divalent metal-doped MFe_2O_4 (M ≅ Co, Ni, Zn, Mg, and Sn) MNPs prepared *via* the Ko-precipitation Hydrolytic Basic (KHB) methodology and assess their magneto-thermal abilities. The physiochemical, structural, morphological, compositional, and magnetic properties of the doped ferrites were fully characterized using various techniques mainly TEM, XRD, EDX, FTIR, and VSM. The obtained doped MNPs exhibited stabilized quasi-spherical sized particles (10–17 nm), pure well-crystallized cubic spinel phases, and high saturation magnetizations (M_s = 26–81 emu g^{-1}). In response to a clinically-safe alternating magnetic field (AMF) (f = 332.8 kHz and H = 170 Oe), distinctive heating responses of these doped ferrites were attained. Hyperthermia temperatures of 42 °C can be reached very fast in only ~5 min, with heating temperatures slowly increasing to reach up to 55 °C. The highest heating performance was observed for PVP-$NiFe_2O_4$ and the lowest for PVP-Sn-doped NPs (SAR values: PVP-$NiFe_2O_4$ > PVP-$CoFe_2O_4$ > PVP-$ZnFe_2O_4$ > PVP-$MgFe_2O_4$ > PVP-$SnFe_2O_4$). This trend was found to be directly correlated to their observed magnetic saturation and anisotropy. Heating efficiencies and specific SAR values as functions of concentration, frequency, and amplitude were also systematically investigated. Finally, cytotoxicity assay was conducted on aqueous dispersions of the doped ferrite NPs, proving their biocompatibility and safety profiles. The PVPylated metal-doped ferrite NPs prepared here, particularly Ni- and Co-doped ferrites, are promising vehicles for potential combined magnetically-triggered biomedical hyperthermia applications.

Received 1st March 2024
Accepted 6th May 2024

DOI: 10.1039/d4ra01600a

rsc.li/rsc-advances

1. Introduction

Magnetic iron oxide nanoparticles (MNPs) have been widely used in biomedical theranostics as magneto-responsive nanoprobes for multimodal imaging, magnetic drug targeting, magnetic resonance imaging, and magnetic fluid hyperthermia.[1–4] Particularly, in magnetic hyperthermia an implanted magnetic material is utilized under an external alternating magnetic field (AMF) to dissipate heat from MNPs in the area of concern.[5] This approach has become one of the promising potential treatments for cancer as it enables the destruction of malignant solid tumors by ablation (T = 45–46 °C) or mild heating (T = 40–45 °C) with minimal side effects. MNPs and their doped ferrites (MFe_2O_4; where M = iron (Fe), cobalt (Co), nickel (Ni), zinc (Zn), or magnesium (Mg), *etc.*) have been successfully used in this regard.[6,7] They own ferromagnetic and superparamagnetic properties that make their magnetic moments align with the applied magnetic field and, hence, release energy as heat, cooking and killing the target cells selectively.

Among the various MNPs, magnetite (Fe_3O_4) is the most commonly studied material for cancer hyperthermia treatment due to its low toxicity, ease of synthesis, and FDA approval.[8,9] It is clearly evident, from our and other reports,[10–13] that the heating efficiencies of MNPs are affected by several parameters such as size and shape of the NPs, saturation magnetization

[a]*Department of Chemistry, College of Science, University of Bahrain, Sakhir 32038, Bahrain. E-mail: khboubbou@uob.edu.bh; Tel: +973 17437506*

[b]*Department of Physics, College of Science, Imam Mohammad Ibn Saud Islamic University (IMISU), Riyadh 11623, Saudi Arabia. E-mail: mamamin@imamu.edu.sa; Tel: +966 112594627*

[c]*Department of Physics, College of Science, University of Bahrain, Sakhir 32038, Bahrain*

[d]*Medical Research Core Facility and Platforms (MRCFP), King Abdullah International Medical Research Center/King Saud Bin Abdulaziz University for Health Sciences (KSAU-HS), King Abdulaziz Medical City (KAMC), NGHA, Riyadh, Saudi Arabia*

[e]*School of Physics and Astronomy, University of Nottingham, Nottingham, NG7 2RD, UK*

† Electronic supplementary information (ESI) available. See DOI: https://doi.org/10.1039/d4ra01600a

(M_s), magnetic anisotropy constant, NP concentration, surface modification as well as the amplitudes and frequency of the applied magnetic field under various experimental conditions. In order to keep improving on the heat dissipated by MNPs, typically computed by specific absorption rate (SAR) and intrinsic loss power (ILP) values, one approach often consists of tuning the magnetic properties of these MNPs by doping the construct with divalent transition metals to prepare ferrite NPs.[14–17]

Metal Ferrites MFe_2O_4 (M = Co, Ni, Zn, Mg *etc.*) are well-studied for magnetic hyperthermia applications, though, with limited outcome.[15,18–21] The unique ferrite structural stability properties allow more controllable physiochemical properties. This is due to the ability of atom transition between the tetrahedral and octahedral sites within the crystal, which causes alteration in magnetic properties.[22] Moreover, applying different divalent transition metals within the ferrite structure produces distinct magneto-thermal properties depending on their atomic specification (ionic radius and ionic strength) and the amount of ions doped. Hence, different metal-doped spinel ferrite structures own unique properties such as grain and crystallite sizes as well as different ranges of saturation magnetization, which in turn affects the magnetic behavior and heating efficiencies.[23,24] For instance, Co-ferrite ($CoFe_2O_4$) NPs is one of the most studied ferrites for thermal applications due to its good chemical stability, significant intrinsic magneto-crystalline anisotropy, and moderate magnetic saturation.[25,26] Moreover, very good heating abilities of various sizes and shapes of trevorite (Ni-Fe_2O_4) NPs were reported,[27,28] with the possibility of tuning the SAR values by changing experimental settings. Spinel Zn-ferrites ($ZnFe_2O_4$) were also applied successfully either alone or mixed with Co or Ni in limelight to find their use as heat mediators in magnetic hyperthermia.[29–31] Likewise, magnesioferrite ($MgFe_2O_4$) NPs or mixed Mg ferrites were also explored as candidates for hyperthermia with reasonably good SAR values.[32] The use of spinel ferrite NPs with best saturation magnetization (M_s) and heating potentials is key to improve magnetic hyperthermia efficacies. Nonetheless, most of the reported ferrites in the literature are prepared without any appropriate coating, rendering the usage of such materials impractical for biomedical applications due to their reduced biocompatibility, low aqueous dispersity, and high sensitivity to oxidation.

It is of immense importance that ferrite NPs are incorporated with proper polymers to enhance their biocompatibility and stability in physiological media, lower their toxicities, minimize their agglomeration and solution precipitation, and boost their controlled heat dissipation.[29] The polymer matrix typically functions as a thermal insulator, preventing excessive heat dissipation and concentrating the generated heat in the target tissue.[33–36] This controlled and localized heating allows for more accurate treatment while reducing damage to neighboring healthy tissues and increasing hyperthermia's therapeutic efficiency. Furthermore, the use of polymer coating the metal cores enables multifunctionality, where polymers can be made to have a variety of features, including biodegradability, drug-loading/release, and temperature-responsiveness. For hyperthermia applications, it has been shown that surface functionalization and polymer coating can result, in certain cases, in enhanced heat transmission.[33,37,38] For instance, we have shown in our previous work the superior heating power of PVP-coated Fe_3O_4 NPs over other employed polymeric-Fe_3O_4 NPs (*i.e.* PEG, Dextran, Hyaluronic acid, and PAA).[33] PVP is a well-known non-ionic water-soluble polymer that is widely used in the pharmaceutical industry as dispersant, binder, and suspender. Thus, for clinical hyperthermia applications, synthesis of high-quality colloidal PVP-coated doped ferrites and decoding their specific magneto-thermal heating capabilities are highly demanded.

Herein, a panel of PVPylated metal-doped MFe_2O_4 (where M ≅ Co, Ni, Zn, Mg, and Sn) ferrites was prepared using our Co-precipitation Hydrolytic Basic (KHB) methodology to be utilized for magnetic hyperthermia. We first evaluated the physiochemical, morphological, compositional, and magnetic properties of the doped ferrites using various spectroscopic and electronic techniques. We then mapped the magneto-thermal responses of the various PVPylated doped ferrites in response to clinically-safe AMF (f = 332.8 kHz and H = 170 Oe), computing SAR and ILP values. We also investigated the effects of concentration, field amplitude, and frequency on the self-heating abilities of a doped ferrite. Finally, cytotoxicity viability assay was conducted on aqueous dispersions of the doped ferrite NPs, proving their biocompatibility and low toxicity. To the best of our knowledge, this is the first report systematically studying the heating efficiencies of various PVP-capped doped MFe_2O_4 NPs for hyperthermia applications under safe clinical magnetic field conditions.

2. Experimental section

2.1. Materials and methods

All chemicals and solvents were obtained from commercial suppliers and used as supplied without further purification. Iron(III) chloride hexahydrate ($FeCl_3 \cdot 6H_2O$), iron(II) sulfate heptahydrate ($FeSO_4 \cdot 7H_2O$), cobalt(II) chloride hexahydrate ($CoCl_2 \cdot 6H_2O$), nickel(II) chloride hexahydrate ($NiCl_2 \cdot 6H_2O$), zinc(II) chloride hexahydrate ($ZnCl_2 \cdot 6H_2O$), tin(II) (Stannous) chloride dihydrate ($SnCl_2 \cdot 2H_2O$), magnesium chloride hexahydrate ($MgCl_2 \cdot 6H_2O$), polyvinylpyrrolidone (PVP K30 Mw ~40 000), and 28% ammonium hydroxide (NH_4OH) were all purchased from Fisher Scientific. All reactions were carried out under inert nitrogen atmosphere.

For biological assays, Dulbecco's Phosphate Buffered Saline (DPBS), Phosphate Buffered Saline (PBS), Advanced Dulbecco's Modified Eagle Medium (DMEM), Phenol-red free DMEM, Fetal Bovine Serum (FBS), Hoechst 33 342 stain, L-Glutamine, and Penicillin-Streptomycin (Pen-Strep) were all purchased from Invitrogen. MTT (Thiazolyl Blue Tetrazolium Bromide) powder was purchased from Bioworld, USA. All cell lines were purchased from the American Type Culture Collection (ATCC) and grown in Advanced DMEM supplemented with 10% FBS and 1% Penicillin/Streptomycin. Human cancerous cells used in this study are: MDA-MB-231 (metastatic breast cancer cell line) and KAIMRC1 (naturally immortalized KAIMRC1 breast

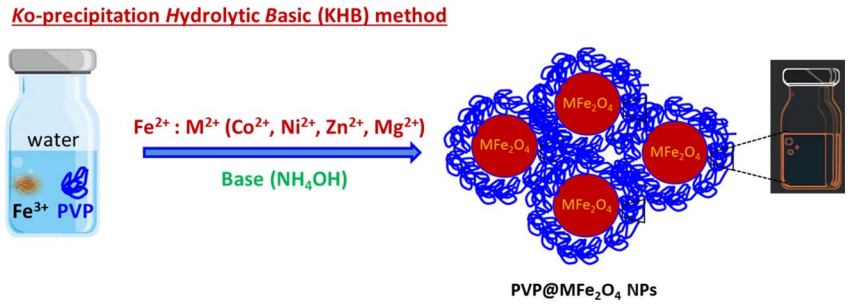

Fig. 1 Schematic diagram for the preparation of PVP-coated metal-doped MFe_2O_4 (M = Co, Ni, Zn, Mg, Sn) NPs using Ko-precipitation hydrolytic basic (KHB) methodology.

cancer cells isolated from a 62 year-old Arab female suffering from stage IIB breast cancer). All experiments were conducted in triplicates and mean.

2.2. Characterization

X-ray diffraction (XRD) using Rigaku Uitima IV equipped with Cu-Kα radiation source (0.15418 nm) with angle ranging from 10° to 80° and the crystal structure parameters were obtained through Rietveld analysis. The morphology of the samples was studied by means of transmission electron microscope (TEM). TEM micrographs of the MNPs were obtained using a Titan 300 kV ST (FEI) electron microscope. Prior to TEM imaging, we treated the TEM grids with plasma to remove organics and dust. For TEM imaging, a few drops of the doped MFe_2O_4 samples were drop-casted on the TEM grids and dried under vacuum. Elemental compositional analyses were performed on the samples using scanning electron microscopy-energy dispersive X-ray (SEM-EDX) processed using SEM-SERON-AIS1800C model equipped with EDX® system and core-loss electron energy loss spectroscopy (EELS) in nanoscale. Fourier transform infrared (FTIR) spectra (400–4000 cm^{-1}) were recorded as KBr pellet forms using Shimadzu IR Affinity-1. Magnetic characterizations were performed using vibrating sample magnetometer (VSM) with 1.8 T magnets at ambient temperature.

2.3. Preparation of PVP-coated MFe_2O_4 NPs by KHB method

All MNPs were prepared using our previously reported KHB method. $FeCl_3 \cdot 6H_2O$ (0.30 g) was mixed with PVP (0.2 g) dissolved in water (10 mL) and stirred for few minutes at 80 °C under nitrogen. $Fe^{2+}:M^{2+}$ (0.1 g : 0.1 g) dissolved in water was then injected into the above solution. Ammonium hydroxide NH_4OH 28% (~3 mL) was slowly added where the solution turned black-brick colored depicting the formation of doped MNPs and stirring was continued for 3 h. The NP suspensions were then purified *via* centrifugation (4500 rpm, 5 min), washed several times with isopropanol, ethanol, and water, and finally re-dispersed in water to afford stable aqueous dispersions of PVP-coated doped MFe_2O_4 NPs. For the preparation of Fe_3O_4 NPs, same procedure was followed using 0.2 g of Fe^{2+}. For samples prepared with higher metal doping, same procedure was followed using $Fe^{2+}:M^{2+}$ (0.05 g : 0.15 g).

2.4. Evaluation of heating efficiencies

The heating efficiency of the samples was performed using a commercial system "Nanotherics Magnetherm" as reported in our previous works.[13,18,33] Different concentrations (10, 7.5, 5, and 2.5 mg mL^{-1}) of doped MNPs have been investigated at 170 Oe and 332.8 kHz for the field amplitude and frequency, respectively. The samples were dissolved in distilled water and sonicated for 10 min and the temperature increase of the samples was then recorded for 15 min.

2.5. Cell viability assay

Cell viability of breast cancer MDA-MB231 and KAIMRC1 cells exposed to different concentration of MNPs was determined using MTT assay. The cell lines were seeded in a 96-well plate at a density of 5×10^5 cells per well and incubated in 95%/5% humidified air/CO_2 at 37 °C. After overnight incubation, cells were treated with various concentrations of control and metal-doped samples in 100 μL of supplemented DMEM. After 48 h of incubation, the medium was removed, and the cells were washed with PBS. Then, 5 μL of MTT reagent (5 mg mL^{-1}) was added to each well and kept for 4 h at 37 °C in the incubator. The supernatant was then removed, and 100 μl of dimethyl sulfoxide (DMSO) was added to each well. The absorbance was measured on the Molecular Devices Spectrophotometer absorbance reader at 590 nm. The percentage of viable cells was calculated as the ratio of the absorbance of the treated group divided by the absorbance of the control group multiplied by 100.

3. Results and discussion

3.1. Preparation and characterization of MFe_2O_4 MNPs

Most of the magneto-thermal properties of ferrites strongly depend on the structure, morphology, and size of the NPs, which are directly related to the method of preparation. Several methods have been proposed to synthesize various kinds of ferrites, including sol–gel, microemulsion, reverse-micelle, solvo(hydro)thermal, sonochemical, combustion, forced hydrolysis, and thermal decomposition.[39,40] However, most of these methods require expensive and often toxic reagents, tedious and complicated synthetic steps, high reaction temperatures, and long reaction times. Although the typical

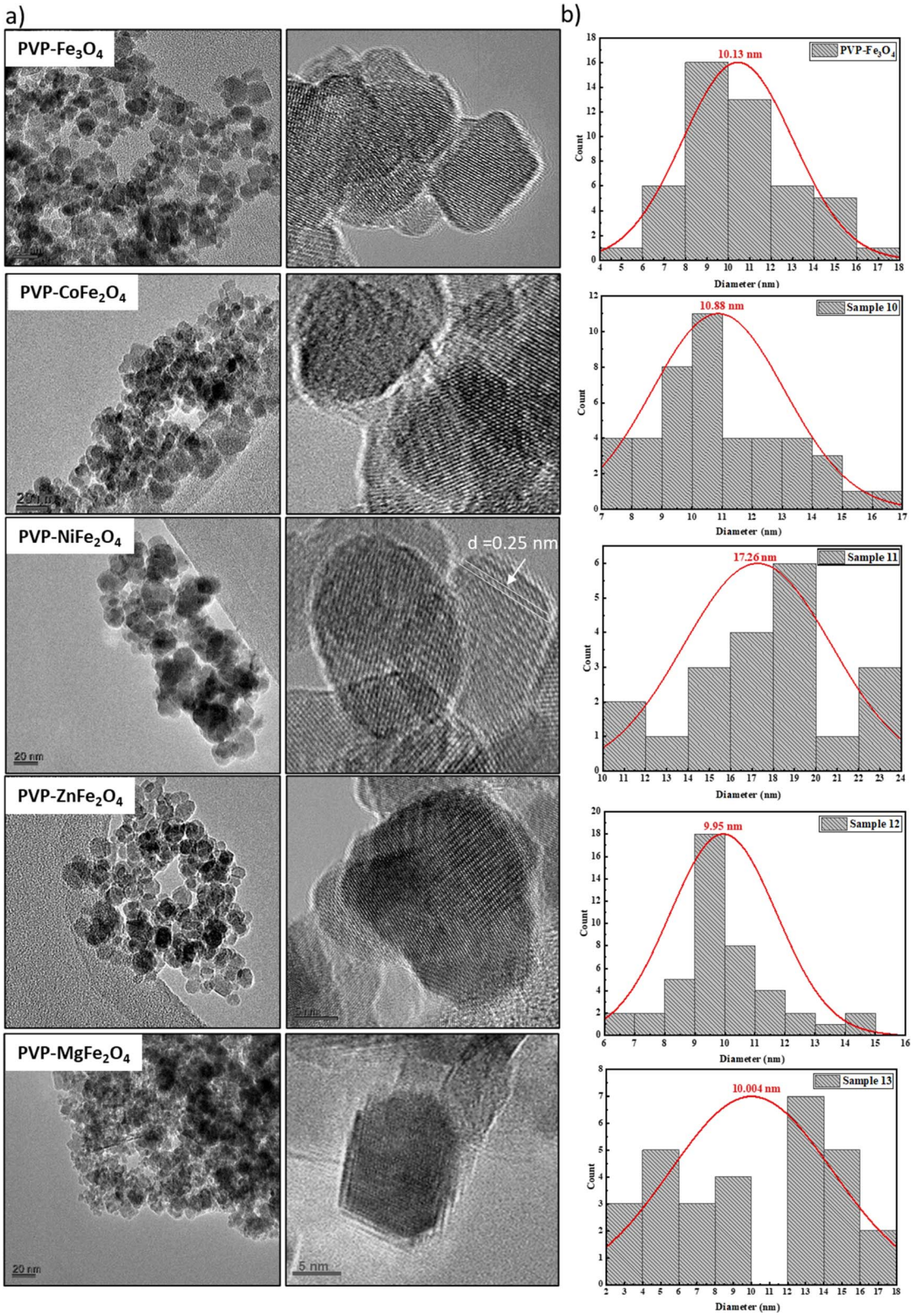

Fig. 2 (a) TEM and HR-TEM images of the various PVP-capped metal-doped MFe_2O_4 samples; (b) corresponding particle-size distribution from the TEM images.

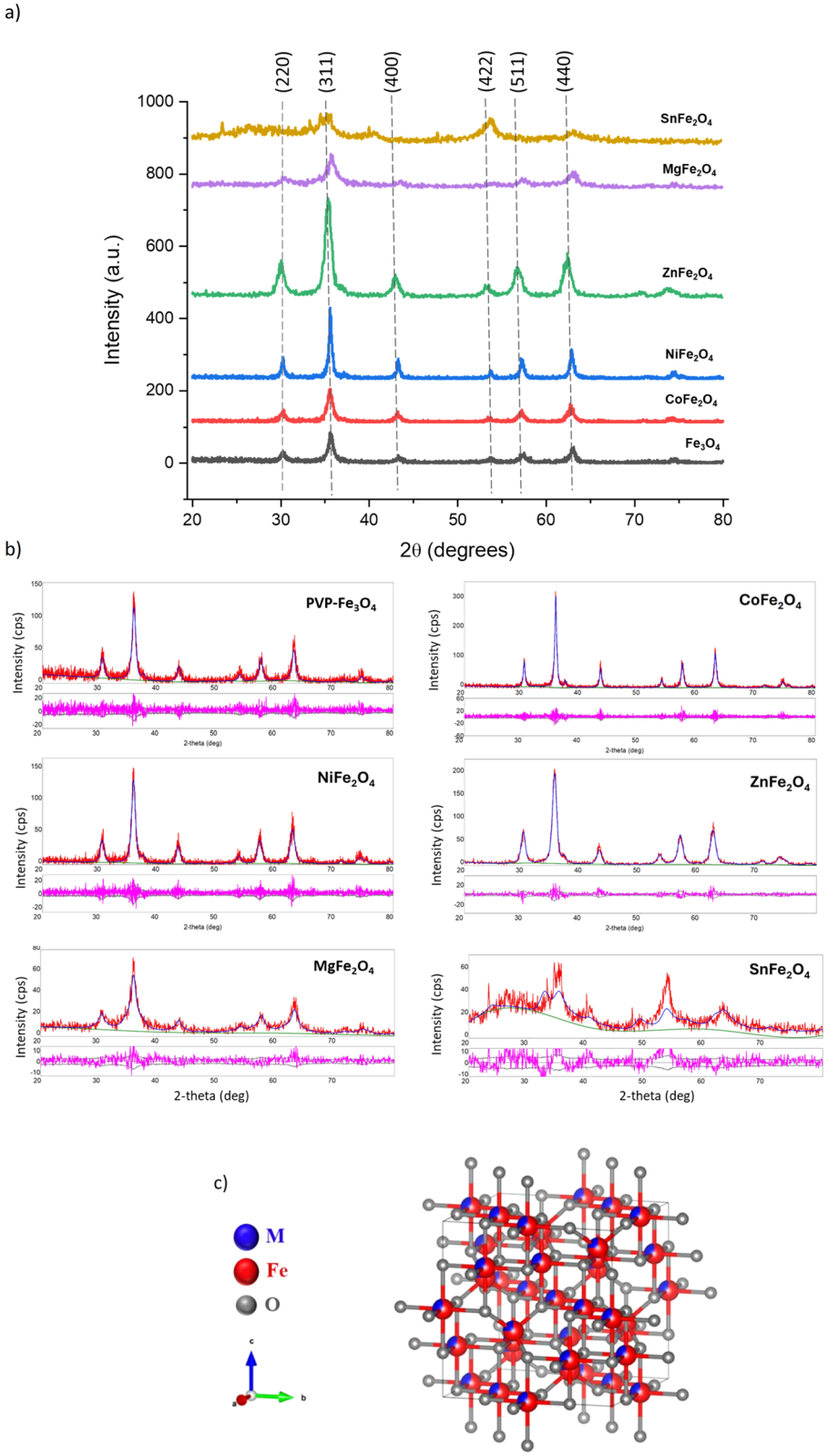

Fig. 3 (a) Powder X-ray diffraction patterns of the various PVPylated metal doped MFe_2O_4 samples. (b) Rietveld refinement profiles of XRD data of all samples. The red line represents the observed experimental data, and the blue line represents the Rietveld refinement fit. The lower pink curve is the difference between the observed and calculated at each step. The refinements clearly depict the excellent agreement between the observed and calculated patterns. (c) Structural model of the primitive unit cell deduced from Rietveld analysis.

chemical co-precipitation route is the most convenient, economic, scalable, and less time-consuming, however, in previous reports it was always observed that there exist some undesirable intermediate phases, which led to poor magnetic properties, low crystallinity, and irregular shape for the derived ferrite NPs.[25] Herein, highly monodispersed MFe_2O_4 ferrite NPs with relatively homogeneous sizes were prepared using our previously reported KHB methodology as illustrated in Fig. 1. Briefly, sequential *in situ* basic hydrolytic precipitation of iron salts (Fe^{3+} and M^{2+} : Fe^{2+}; 1 : 1) in the presence of PVP afforded stable aqueous dispersions of PVPylated metal-doped MFe_2O_4 NPs. The obtained doped ferrites were characterized by various electronic and spectroscopic techniques including TEM, XRD, FTIR, EDX, and VSM. These techniques clearly revealed the structure, morphology, and magnetization of the as-synthesized MFe_2O_4 NPs. TEM images (Fig. 2a) clearly indicated the quasi-spherical morphology of all ferrite NPs, with average sizes of 10 nm except for Ni ferrite NPs (sizes ~17 nm) as depicted by their corresponding particle size-distribution (Fig. 2b). High-resolution TEM (HR-TEM) indicates that the NPs show close-packed 2D array of relatively uniform sized particles clearly showing the interfringe lattices of the NPs. In fact, the distance between two adjacent lattice fringes obtained by HR-TEM analysis of a single nanocrystal is calculated to be ~0.25 nm corresponding to the lattice spacing of (311) planes of magnetite.[41] To interpret the crystalline structure and identify the phase of the obtained ferrites, XRD was performed. XRD patterns of all MFe_2O_4 samples are illustrated in Fig. 3a, showing well-crystallized single-phase inverse spinel structures. Well-defined peaks are observed for each spectrum indicating the crystalline nature of the samples. For all samples, main peaks were defined at (220), (311), (400), (422), (511), (440), and (533) which are related to the spinel structure. Very slight peak shifting, particularly for $MgFe_2O_4$ and $SnFe_2O_4$ samples, was observed, in agreement with previous reports.[42] Both Co and Ni ferrite possess a fully inverse structure due to the chemical nature of Ni^{2+} and Co^{2+} which tend to occupy octahedral sites while Fe^{3+} occupy tetrahedral ones.[43] Rietveld analysis of these XRD patterns confirmed the formation of pure MFe_2O_4 cubic spinel phases with space group *Fd3m* for $NiFe_2O_4$, $CoFe_2O_4$, $ZnFe_2O_4$, and $MgFe_2O_4$ which matches well with JCPDS # 01-071-3850, # 01-074-6402, # 01-071-5149, and # 01-071-4919, respectively. The refinements show an excellent agreement between the observed and calculated patterns (Fig. 3b). No additional peaks have been observed suggesting that the synthetic method leads to the formation of a pure spinel ferrite phase. From Rietveld analysis of XRD results, the crystallite size, microstrain, and lattice parameters of all samples were calculated (Table S1†). Different sizes of crystals were formed depending on the metal ferrite ranging from ~5 nm for $MgFe_2O_4$ to 18.5 nm for $NiFe_2O_4$. Such variation in crystallite size between different metal ferrites might be due to the difference in the ionic radii of the dopant metals.[44] The lattice parameters ($A = 8.344$, $B = 8.344$, and $C = 8.344$) for all doped samples were only slightly altered. The unit cell of the MFe_2O_4 ferrite structures deduced from Rietveld shows that iron ions are tetrahedrally and octahedrally coordinated to oxygens, where doping with M^{2+} did not alter much either the crystal structure or the lattice parameter (Fig. 3c). This is expected as the substitution of Fe^{3+} ions by very small amounts of M^{2+} ions (Fe^{3+} : M^{2+}; 3 : 1) would not induce geometrical distortion in the unit cell.[18] Even when the percentage of doping metal was slightly increased, no difference in XRD peaks was observed, pinpointing the formation of a well-resolved pure crystalline MFe_2O_4, however, absence of Fe^{2+} distorted the crystalline phase (Fig. S1†). Regarding Sn-doped sample, the XRD indicated less crystallinity as the peaks were not sharp. The Rietveld analysis showed its best match with $Sn_{0.5}Fe_{2.5}O_4$ phase matching well with JCPDS # 01-071-0695. It is believed that $Sn_xFe_{3-x}O_4$ ($x = 0$ to 1) takes a mixed spinel structure, where both the Sn^{2+} and Fe^{3+} cations are distributed in A and B sites within the ferrite crystal lattice.[45] Therefore, such differences in site occupancies between Sn and Fe ions within the ferrite structure may be the reason of this variation in their crystalline phase. Next, SEM-EDX analyses was conducted to verify the elemental composition of the different doped ferrite samples (Fig. 4a). Interestingly, the elemental composition performed on selected SEM areas confirmed the purity of the obtained ferrites with corresponding atomic percentages of 9–12.5% for the doped metal (*i.e.* Co, Ni, Zn, Mg, and Sn), ~25% Fe, 50–55% O, and 7.5–11% C (Table S2†). These results nicely corroborated the pure XRD MFe_2O_4 phases obtained by Rietveld analysis. STEM-EELS mapping was further performed on a selected PVP-Co-Fe_2O_4 NP sample to further elucidate their structure. The spatial distribution of each component within the NPs was investigated using the spectrum imaging (SI) method,[46] and the obtained elemental mappings of the elements are shown in Fig. 4b. The uniform distribution was observed in the generated map of each element. Each sample's black and white image represents the High Angle Annular Dark Field (HAADF) imaging, while the red, green, cyan, and blue colors represent Fe, O, C, and Co elements, respectively. The presence of only Fe, O, C, and Co peaks without any additional elements reveal the high purity of the obtained doped ferrites.

FTIR analysis was then conducted to further validate the formation of PVP-coated MFe_2O_4 NPs (Fig. 5). The presence of iron oxide (Fe_3O_4) in the core was clearly evident by the Fe–O stretching bands at 560 and 620 cm^{-1}, which appeared as one broad peak ~560–600 cm^{-1} for the MFe_2O_4 because of metal doping the crystallites. The distinctive peaks at 2850 and 2920 cm^{-1} clearly depict the symmetric and asymmetric C–H stretching modes of PVP coating, while the broad peak at ~3400 cm^{-1} is ascribed to the O–H stretching vibration of hydroxyl groups on MNPs. Another major signature peak is the stretching vibration of C=O carbonyl evident at ~1635 cm^{-1}. The carbonyl of free PVP polymer typically appears at 1660 cm^{-1}.[47,48] This shift from 1660 cm^{-1} to 1635 cm^{-1} confirms the functionalization of MNPs with PVP *via* intermolecular hydrogen bonding between the carbonyl group of PVP and the protonated hydroxyl groups on MNP surfaces. Moreover, PVP is well-known to adsorb on the ferrite nanocrystals *via* coordinative bonds between the pyrrolidone molecules and the metal ions, where the donated lone pairs of both nitrogen and oxygen atoms

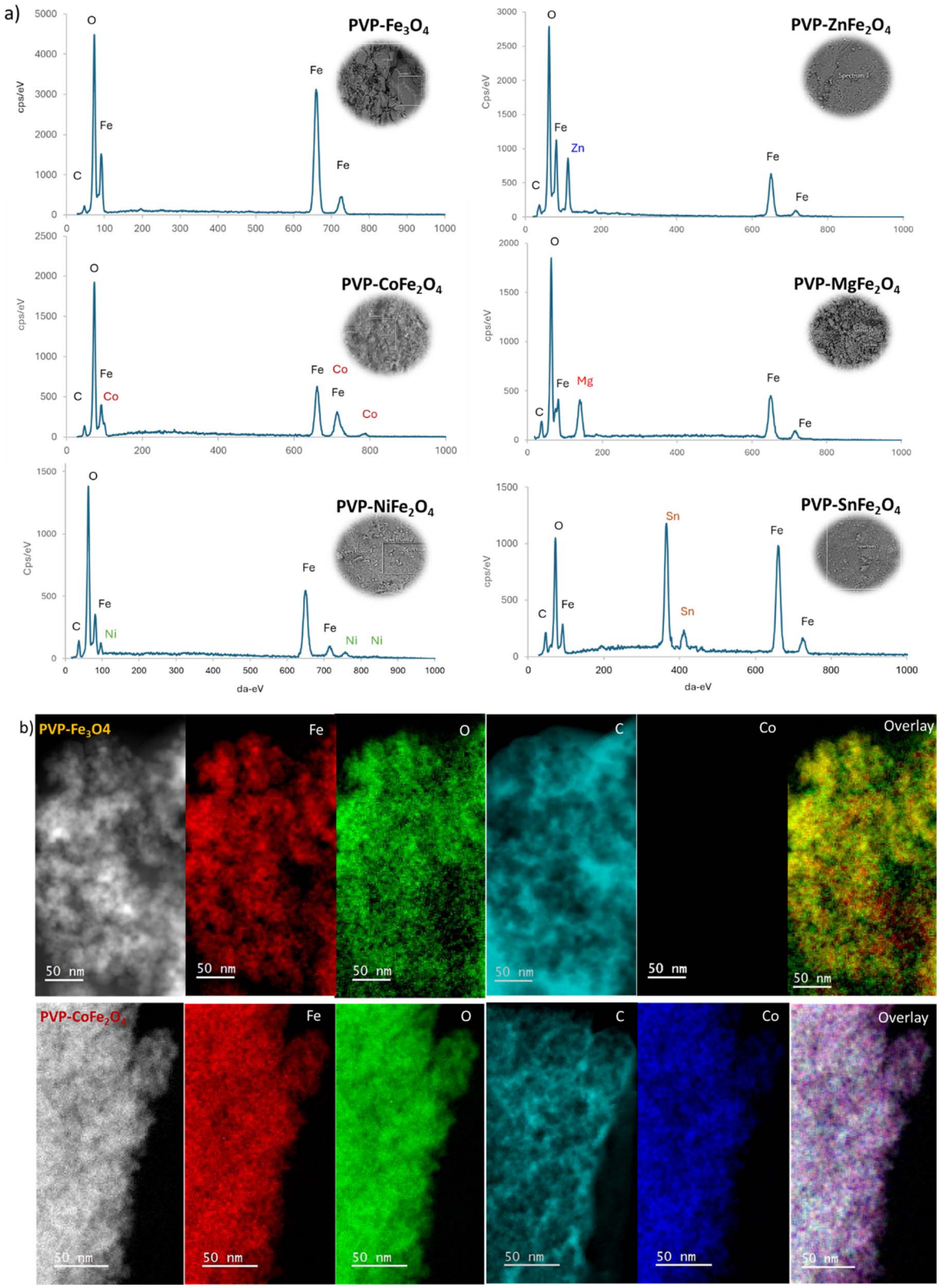

Fig. 4 (a) SEM-EDX elemental analysis of the various PVPylated metal doped ferrites. (b) STEM-EELS elemental mapping of PVP-Fe_3O_4-MNPs and PVP-$CoFe_2O_4$-MNPs. The results clearly show the successful doping and purity and of the samples.

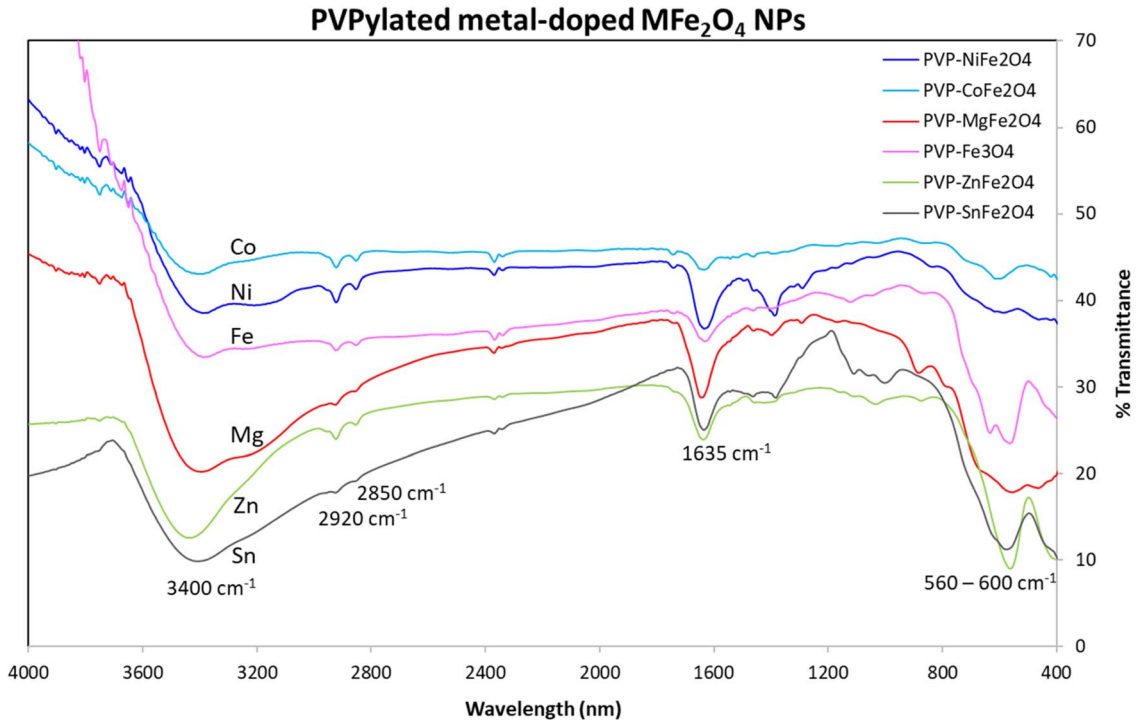

Fig. 5 FTIR for the various PVPylated metal-doped MFe_2O_4 NPs clearly showing the successful polymer coating the different nanoferrites (Fe–O stretching at 560–620 cm^{-1}) with distinctive peaks at 2850, 2920 cm^{-1} and 1635 cm^{-1} corresponding to C–H and C=O stretching vibrations of PVP.

form complex with Fe^{3+} ions.[49] All these results clearly indicate the successful coating of MFe_2O_4 ferrite NPs with PVP.

3.2. Magnetic properties

To determine the magnetic behavior of the doped ferrites, field-dependent magnetizations were conducted. The polymer coating and metal doping can both have dominant effects on magnetization and, hence, the heating efficiencies of doped ferrite NPs. Fig. 6a depicted the hysteresis loop (M–H) of the as-synthesized doped MNPs at 300 K, while the saturation magnetization (M_s), coercivity (H_c), and remanence (M_r) values deduced from the loops are summarized in Table 1. It can be observed that all ferrite NPs behave as ferromagnetic/superparamagnetic with small and almost negligible coercivity and remanence, except for $CoFe_2O_4$ NPs (Fig. 6b). Among the five nanoferrites, Co-doped sample revealed the highest coercivity and remanence ($M_r = 9.6$ emu g^{-1} and $H_c = 218$ Oe), which is attributed to the strong ferromagnetic and anisotropic nature of cobaltous ions (Co^{2+}) at the octahedral sites which is not able to quench the orbital magnetic moment leading to strong L-S coupling.[50] This is in accordance with many previous studies showing that $CoFe_2O_4$ is a semi-hard magnetic material with high coercivity and moderate magnetization.[26,50,51] The M_s magnetization obtained for the PVP-$NiFe_2O_4$, PVP-$CoFe_2O_4$NPs, PVP-$ZnFe_2O_4$, PVP-$MgFe_2O_4$, and PVP-$SnFe_2O_4$ ferrite NPs were found to be equal to 80.74, 66.17, 38.78, 26.26, 4.26 emu g^{-1}, respectively. As evident the highest saturation magnetizations were found for PVPylated Ni and Co-doped samples with the lowest obtained for Sn-doped ferrite sample. This general trend in magnetic properties of the doped ferrites is to some extent similar to earlier observation.[45,50,52] The differences between saturation can be caused by several factors such as the type of spinel ferrites in which the synthesized samples are crystallized, the magnetic nature and ionic radii of the divalent cations (*i.e.* Co^{2+}, Ni^{2+}, Zn^{2+}, Mg^{+2}, and Sn^{2+}), their distribution in the octahedral and tetrahedral sites, as well as size of NPs obtained. For instance, Ni and Co ferrites are well known for their high magnetic properties,[53] with ionic radii (~78 pm) which is smaller than Sn (118 pm). Co and Ni are ferromagnetic and interactions between Co or Ni ions spin and the lattice favors the alignment of their spins parallel to the cube edge of the spinel lattice. In addition, both ions induce uniaxial magnetic anisotropy in the magnetization direction which will increase saturation.[54] Other divalent cations are non-magnetic where the insertion of these ions in the octahedral sites will affect Fe-ions interactions and induce decrease in long range magnetic ordering, which explained the low saturation. Furthermore, in our XRD measurements, Ni and Co ferrites exhibited more intense sharper peaks representing large crystals that are occupied by Ni and Co in the octahedral sites in the ferrite cubic lattice. On the other hand, Sn and Mg ferrites prepared with similar synthesis conditions did not reveal high crystallinity. Accordingly, the difference in site occupancies among the different ferrite crystal structure had a major influence on their magnetic properties.[55–57] Importantly, however, the PVP-coated MFe_2O_4 ferrite NPs obtained here have relatively high saturation magnetizations, which are larger than similar polymer-

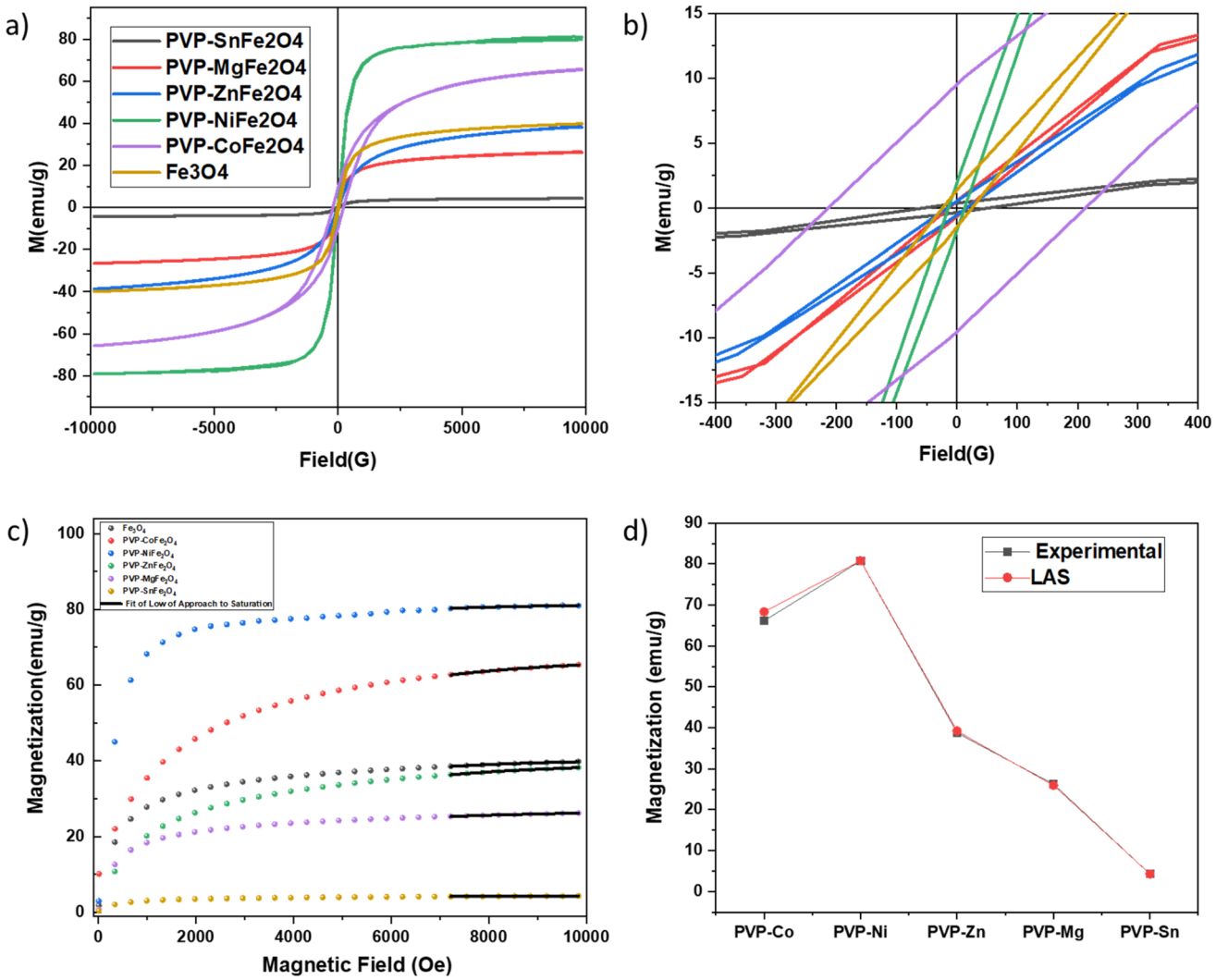

Fig. 6 (a) Field-dependent magnetization hysteresis loops for PVP-ferrite MFe_2O_4 NPs at room temperature; (b) at low field −400 to 400 Oe; (c) law of saturation; (d) saturation deduced from experimental and LAS fitting.

Table 1 Magnetic parameters deduced from M–H curves and law of approach saturation

Experimental					Law of saturation (LAS)	
Sample	H_c (Oe)	M_r (emu)	M_s (emu g^{-1})	M_r/M_s	M_s (emu g^{-1})	K_{eff} (erg cm^{-3})
PVP-Fe_3O_4	26	0.38	39.70	0.010	39.46	4.5857
PVP-$NiFe_2O_4$	13	0.92	80.74	0.011	80.79	12.182
PVP-$CoFe_2O_4$	218	9.60	66.17	0.14	68.35	2.75×10^5
PVP-$ZnFe_2O_4$	18	0.54	38.78	0.014	39.22	3.1038
PVP-$MgFe_2O_4$	16.64	0.50	26.26	0.019	25.97	3.0767
PVP-$SnFe_2O_4$	54.62	0.34	4.26	0.080	4.24	0.50361

coated ferrite MNPs reported in the literature,[49,58–60] indicating high degree of magnetic ordering and crystallinity. For instance, Oulhakem *et al.* reported saturation of 18.43, 13.53, and 0.69 emu g^{-1} for alginate-encapsulated Alg@$CoFe_2O_4$, Alg@$NiFe_2O_4$, and Alg@$ZnFe_2O_4$ respectively.[30] Interestingly, most studies reported decrease of saturation after coating of NPs by organic polymer/matrix,[30,61] while coating with PVP tends to increase the saturation of ferrite NPs (*i.e.* 80.74 emu g^{-1} for PVP-$NiFe_2O_4$) and magnetite NPs.[33]

In addition to M_s, there are three magnetic parameters, which affect the heating ability for hyperthermia application, namely: coercivity, remanence, and magnetic anisotropy

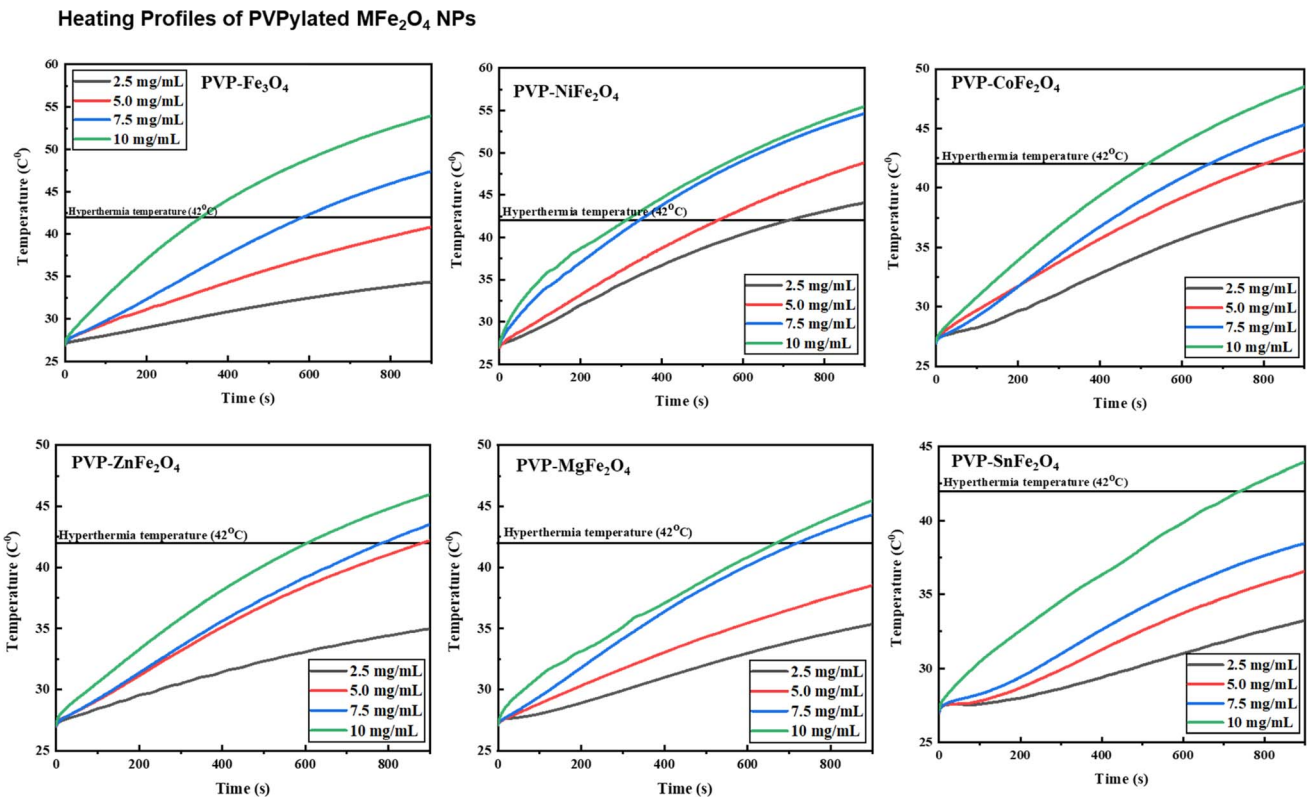

Fig. 7 Heating efficiencies of PVP-ferrites MFe_2O_4 NPs at different concentrations (2.5, 5, 7.5, and 10 mg mL^{-1}) at $H = 170$ Oe, $f = 332.8$ kHz.

constant (K_{eff}). The coercivity is affected by the magnetic nature of the divalent doped cations and as discussed reached the highest value of 218 Oe for PVP-$CoFe_2O_4$ NPs. Regarding the remanence, the ratio (M_r/M_s) values are in the range 0.01–0.14 which deviates largely from the value of 0.5 suggested by Stoner–Wolfahrt's model,[62] for an ensemble of non-interacting single domain magnetic particles distributed randomly. The deviation from the theoretical value $M_r/M_s = 0.5$ could be attributed to the effect of dipolar interactions which reduces the remanence.

Finally, the effective anisotropy constant (K_{eff}) was deduced from the fitting of the experimental magnetization as shown in Fig. 6c by using the following equation:[63]

$$M(H) = M_s\left(1 - \frac{b}{H^2}\right) \quad (1)$$

where b is a parameter which is deduced from the fitting of experimental magnetization with eqn (1). K_{eff} is then determined by eqn (2) as follows:[64]

$$K_{eff} = \mu_0 M_s\sqrt{\frac{15b}{4}} \quad (2)$$

The calculated values of K_{eff} are summarized in the Table 1. It can be observed that the highest value (2.75×10^5 erg cm^{-3}) is obtained for PVP-$CoFe_2O_4$ ferrites which showed the highest coercivity. It can be also noticed that saturation deduced from the fit is slightly different from the experimental values indicating the accuracy of the fitting by LAS (Fig. 6d).

3.3. Magnetic hyperthermia measurements

The heating performance of MNPs is intimately entwined with their structure, size, and magnetic anisotropy. For magnetic hyperthermia, the main challenges lie in obtaining MNPs of specific characteristics: high heating efficiencies with minimal concentrations under clinically safe field exposure. When a magnetic system is subjected to AMF, heat is generated due to certain loss mechanisms, which can be classified as hysteresis and relaxation losses. It was specifically found that SAR values for superparamagnetic/ferromagnetic NPs (almost negligible hysteresis losses) are directly affected by parameters which influence the magnetic moment rotation responsible for heat dissipated through Brownian and Néel relaxation mechanisms.[64–66] Frequency and field amplitude of AMF also have direct effects on the heating efficiencies of the MNPs. For clinical hyperthermia applications and to satisfy medical safety conditions, there are two limitations for the product of the amplitude (H) and the frequency (f) for the applied magnetic field known as the Atkinson–Brezovich limit ($H \times f \leq 4.85 \times 108$ A m^{-1} s^{-1}) and the Hergt's limit ($H \times f \leq 5 \times 10^9$ A m^{-1} s^{-1}).[67,68] Thus, for an efficient clinical utilization of MNPs in hyperthermia, the heat dissipation should be optimized by using minimal dosage of polymer-coated MNPs (to ensure biocompatibility) and high magnetic properties (to guarantee efficient heating) in relatively short times. Therefore, designing tailored doped ferrite NPs that can dissipate heat at low concentrations under different ranges of frequencies and magnetic field is key to achieve a controllable and efficient hyperthermia treatments. Moreover, preparing stabilized well-

dispersed magnetic NPs with high heating efficiencies and SAR values in large quantities in an easy, robust, cheap, and reproducible process is likewise demanded.

The heating efficiencies of PVPylated undoped and doped ferrite NPs dispersed in water under AMF were evaluated. Fig. 7 shows the temperature rise of aqueous dispersions of various doped ferrite NPs at different concentrations under AMF with frequency and amplitude of 332.8 kHz and 170 Oe, respectively. The main parameters that assess self-heating abilities of all MNPs obtained from the temperature rise are summarized in Table 2. As can be observed from Fig. 7, MNPs show high heating abilities and reach magnetic hyperthermia temperatures (42 °C) in relatively short times. Within 15 min, the solution with the highest concentration (10 mg mL^{-1}) reached, noticeably, higher temperatures, in comparison with 7.5, 5, and 2.5 mg mL^{-1} solutions. This dependence of the temperature rise on the concentration of NPs is expected because more heat generators (*i.e.* NPs) are present in the concentrated sample. The temperatures for all the samples slowly increased but did not reach saturation within the 15 min period. During the magnetic hyperthermia treatment, the temperature should be regulated at 42 °C for at least 30 min to kill the malignant tumor, but it should be also kept below 46 °C to prevent normal tissues from burning. Thus, all the tested doped ferrite samples (7.5 and 10 mg mL^{-1}) satisfy these conditions, particularly the PVPylated Ni- and Co Fe_2O_4 NPs. Interestingly, even for lower concentrations of 2.5 mg mL^{-1}, Ni-doped sample indicated a very good temperature rise and reached hyperthermia temperatures.

SAR values, defined as the dissipation heat generated by a unit mass of MNPs, were then determined by eqn (3) as follows:

$$\mathrm{SAR} = \frac{\rho C_w}{\mathrm{Mass_{MNP}}}\left(\frac{\Delta T}{\Delta t}\right) \quad (3)$$

where C_w is defined as the specific heat capacity of water (4.185 J g^{-1} k^{-1}), the density of the colloid is ρ, the concentration of MNPs in the suspension is called $\mathrm{Mass_{MNP}}$ and the heating rate is represented by $\frac{\Delta T}{\Delta t}$. By performing a linear fit of temperature increase *vs.* time at the initial time interval (1 to 15 s), the slope $\Delta T/\Delta t$ is obtained. The calculated SAR values are summarized in Table 2. The relatively high values indicate the good heating capabilities of the prepared ferrite NPs. There is a significant increase of SAR for PVP-$NiFe_2O_4$ NPs compared to other samples, which is relatively higher than that of other similar reported doped magnetic NPs. It can be noted also from the values, that SAR decreases with decreasing concentration of MNPs (since less heat is dissipated), in agreement with our previous work.[33] Comparison of SAR values at 10 mg mL^{-1} concentration (Fig. 8a), shows that PVP-$NiFe_2O_4$ NPs have the highest value (SAR = 54.71 W g^{-1}) followed by PVP-$CoFe_2O_4$ NPs (SAR = 30.57 W g^{-1}), while PVP-$SnFe_2O_4$ NPs indicated the lowest value (SAR = 18.34 W g^{-1}). Difference in SAR values for the doped ferrites can be explained by the effect of many parameters as mentioned earlier such as core sizes, crystallinity, viscosity of the medium, magnetization, anisotropy constant, coercivity, and remanence. However, M_s saturation and K_{eff} anisotropy constant remain the main parameters which directly affects the heating abilities. It is well known that MNPs dissipate heat under AMF mainly through Néel relaxation, where the magnetic moments are reoriented within the particles against an energy barrier with relaxation time τ_N:

Table 2 Heating parameters for the different doped PVP-MFe_2O_4 NPs at various concentrations (H = 170 Oe, f = 332.8 kHz)

Sample	Concentration (mg mL^{-1})	Maximum temperature (°C)	Time needed to reach 42 °C (min)	SAR (W g^{-1}) (2–15 s)	ILP (nHm^2 kg^{-1}) (2–15 s)
PVP-Fe_3O_4	**10**	**53.97**	**5.57**	**30.253**	**0.498**
	7.5	47.42	9.73	21.456	0.353
	5	40.85	Not reaching	27.679	0.456
	2.5	34.37	Not reaching	29.610	0.487
PVP-$CoFe_2O_4$	**10**	**48.53**	**11.15**	**30.575**	**0.503**
	7.5	45.31	11.99	24.031	0.396
	5	43.18	13.35	22.759	0.372
	2.5	38.93	Not reaching	20.897	0.330
PVP-$NiFe_2O_4$	**10**	**55.50**	**5.20**	**54.714**	**0.900**
	7.5	54.66	5.73	51.066	0.840
	5	48.85	8.93	38.622	0.636
	2.5	44.09	11.85	36.047	0.593
PVP-$ZnFe_2O_4$	**10**	**45.99**	**10.07**	**23.495**	**0.387**
	7.5	43.55	13.07	17.165	0.257
	5	42.20	14.41	25.104	0.413
	2.5	35.00	Not reaching	19.909	0.283
PVP-$MgFe_2O_4$	**10**	**45.50**	**8.58**	**20.598**	**0.339**
	7.5	40.18	11.12	19.161	0.354
	5	38.92	Not reaching	14.311	0.230
	2.5	35.16	Not reaching	12.185	0.208
PVP-$SnFe_2O_4$	**10**	**43.98**	**12.35**	**18.345**	**0.302**
	7.5	38.90	Not reaching	12.874	0.212
	5	35.47	Not reaching	7.0810	0.116
	2.5	33.76	Not reaching	9.610	0.187

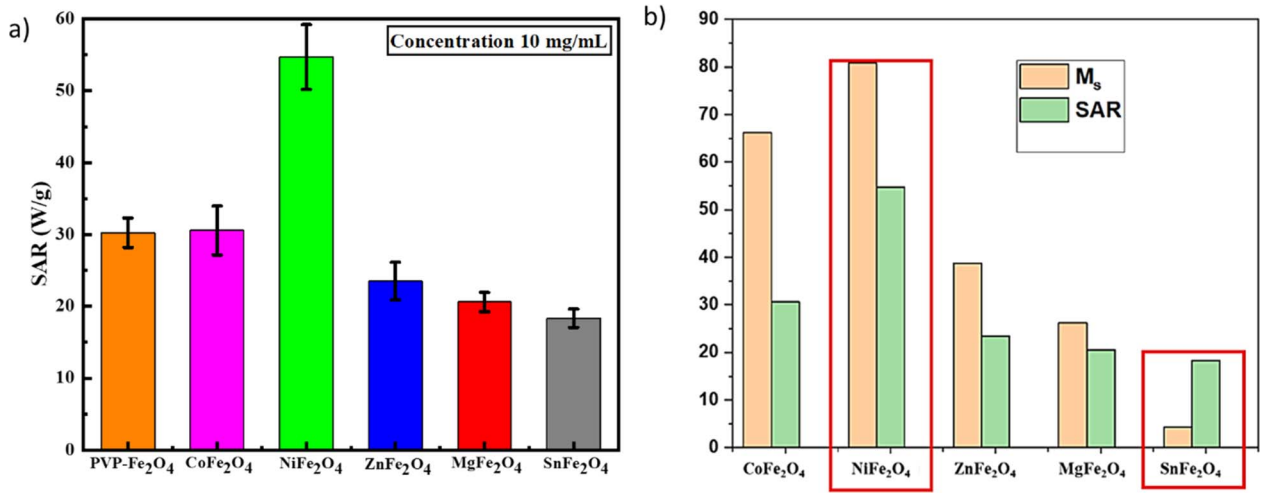

Fig. 8 (a) Calculated SAR values for the different doped samples at 10 mg mL; (b) correlation between magnetic saturation and SAR values. Standard deviation represents three SAR measurements.

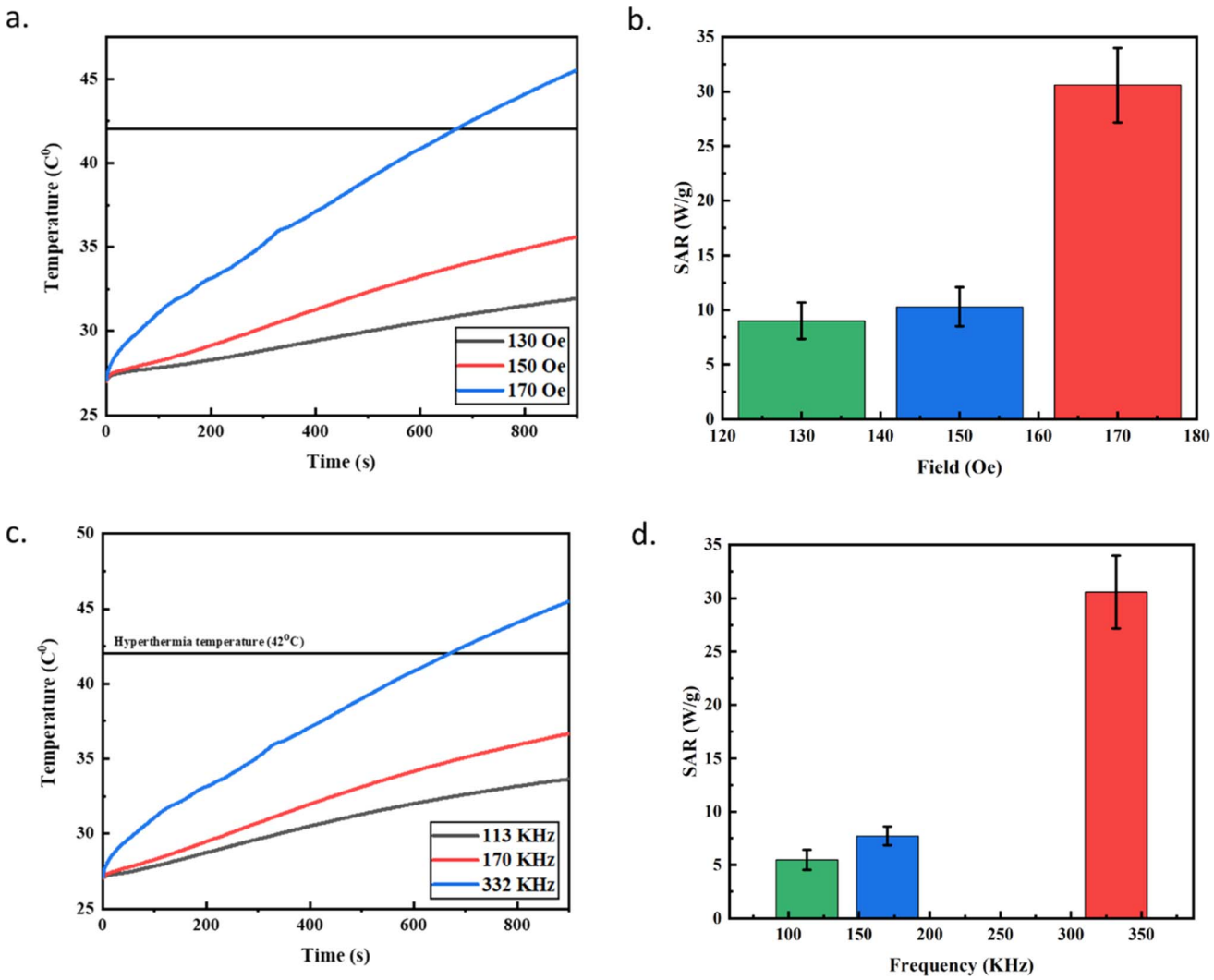

Fig. 9 Effects of the field amplitude and frequency on self-heating ability of PVP-$NiFe_2O_4$ MNPs (10 mg mL^{-1}). (a) Temperature rise at different field amplitude and fixed frequency $f = 332$ KHz and (b) corresponding SARs values; (c) temperature rise at different frequencies and fixed field of $H = 170$ Oe and (d) corresponding SAR values.

$$\tau_N = \tau_0 e^{K_{eff}V/k_BT} \quad (4)$$

where k_B is the Boltzmann constant, τ_0 is the time constant, K_{eff} is the magnetic anisotropy constant, and V is the volume of the nanofluid. As shown in eqn (4), increasing the anisotropy constant will increase relaxation time and subsequently the heat dissipated by the MNPs.[69] Thus the enhanced magnetic anisotropy and saturation in Ni- and Co-doped samples well-explain their high heating abilities. The decrease of heating observed for other doped ferrites could be attributed to the increase in interparticle dipolar interactions, which leads to reduction of Néel–Brownian relaxation and, hence, SAR. Fig. 8b impeccably shows the direct correlation between SAR and M_s values, where MNPs with the highest magnetic saturation (PVP-$NiFe_2O_4$ NPs) and relatively high anisotropy constant resulted in the highest SAR, while the one with lowest saturation and magnetic anisotropy is recorded for PVP-$SnFe_2O_4$ NPs. Thus, it can be clearly concluded that there are optimal parameters that should be produced (size, magnetization, polydispersity, coating, concentration *etc.*) to maximize SAR values for MNPs.

Next, ILP used to compare the heating efficiencies of different MNPs were calculated by using the obtained values of SAR and applying the following equation:

$$ILP = SAR/fH_0^2 \quad (5)$$

where f is the frequency and H_0 is the magnetic field.

The ILP values for different concentrations of doped MNPs under the different sets of experimental conditions and various concentrations are summarized in Table 2. As can be observed, these ILP values are comparable to those reported for magnetite and commercial ferrofluids (0.2–3.1 $nHm^2\ kg^{-1}$),[70] with the highest ILP (0.9 $nHm^2\ kg^{-1}$) attained for PVP-$NiFe_2O_4$ NPs.

As PVP-$NiFe_2O_4$ NPs displayed the best magneto-thermal properties with highest SAR and ILP values, the effects of both field amplitude and frequency on self-heating abilities were investigated. Thus, different combinations of magnetic fields and frequencies were applied. In Fig. 9a, the frequency was fixed at 332 kHz and the magnetic field varied to 130, 150 and 170 Oe. It can be noticed that the temperature rise increases with increasing field amplitude. Magnetic hyperthermia temperature (42 °C) is not reached at 130 Oe, however increasing the magnetic field to 170 Oe caused a clear rise in temperature allowing the reach of 42 °C. SAR values were increased with increasing field amplitude (Fig. 9b). Similar behavior is observed when the frequency was adjusted to 113, 170 and 332 kHz, while the field was fixed to 120 Oe as shown in Fig. 9c and d. Overall, for all applied frequencies, the maximum temperature reached by the NPs is increasing with field amplitude, leading to higher SAR values. As shown previously in eqn (3), the calculation of SAR values depends on the initial slope of temperature rise. All these results indicated that the self-heating properties of the MNPs can be tuned easily by changing the concentration, magnetic field amplitude, and frequency of the AMF. Such tuning depends mainly on the nature of the doping metal, polymer coat, magnetic behavior, particle size and crystallinity, interparticle interactions, sample concentration and dispersing medium. Hence, the synthetic methodology employed to prepare high-quality stabilized colloidal aqueous dispersions of polymer-coated doped ferrites is a kay factor for optimizing their self-heating and magneto-thermal characteristics.

3.4. Cytotoxicity and safety profiles

It is crucial to evaluate the cytotoxicity and safety profiles of the PVPylated ferrite NPs before utilizing them for biomedical magnetic hyperthermia applications. We focused on the formulations which generated the highest heating efficiencies (*i.e.* Ni, Co, and Zn-doped ferrites). Thus, the toxicities of

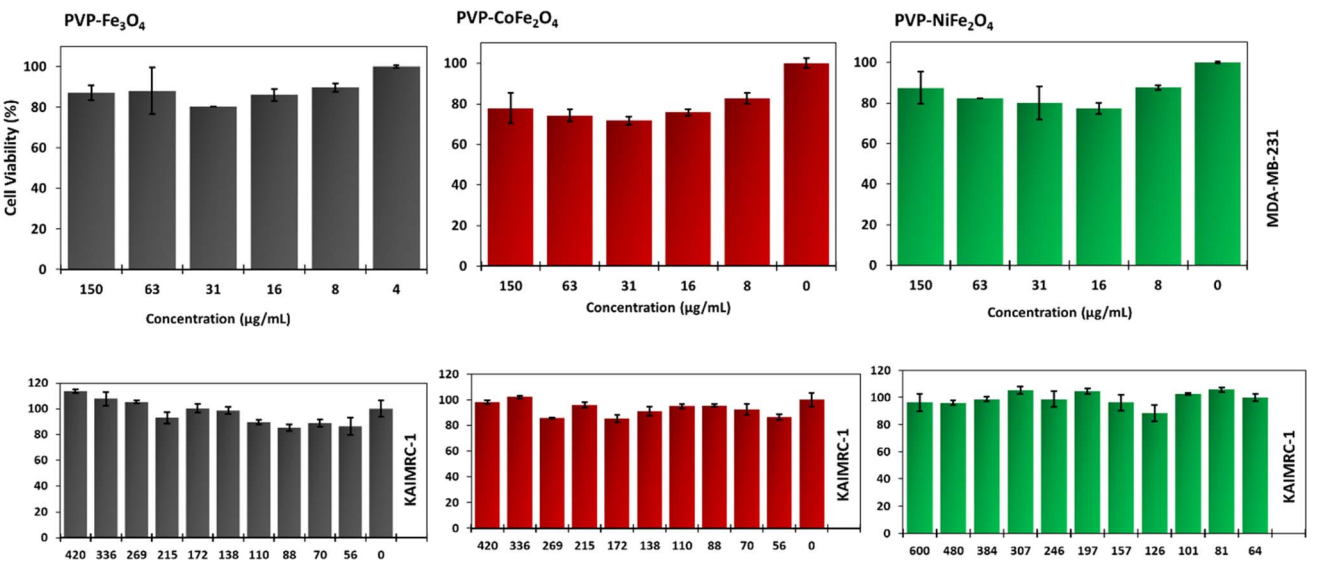

Fig. 10 MTT cell viability assay for different concentrations of doped MFe_2O_4 MNPs against MDA-MB-231 and KAIMRC1 metastatic breast cancer cells. The results clearly depict the low toxicity and biocompatibility of the doped ferrite NPs.

various concentrations of doped ferrites towards a metastatic breast cancer cell lines MDA-MB-231 and KAIMRC-1 (ref. 71) were evaluated using thiazolyl blue tetrazolium bromide (MTT) viability assay. The MTT assay is based on the capacity of the mitochondrial enzyme of viable cells to transform the MTT tetrazolium salt into a violet-bluish colored MTT formazan, which is proportional to the number of living cells present. As can be seen in Fig. 10, all doped ferrites were not toxic to MDA-MB-231 or KAIMRC-1 cancerous cells, even at considerably high concentrations (~70–80% of the cells remained viable). Interestingly, for PVP-Ni-doped MNP, even when treated with concentrations up to 600 μg mL^{-1}, no significant cytotoxicity was observed (>80% of the cancer cells stayed viable). This repeatedly confirms the safety profiles for magnetite and ferrites, reported by us and others, where even using high concentrations of iron oxide NPs are considered to be safe to the cells with no significant cytotoxicity. This is in accordance with the standardized guidelines for MTT assay in ISO-10993-5 where toxicity is defined as less than 70% viability. Thus, combining the good biocompatibility profiles along with the high heating efficiencies attained suggests that the fabricated PVP-capped doped MNPs hold a great potential for magneto-guided *in vivo* hyperthermia applications. Moreover, as mentioned, all results were obtained under experimental condition Hergt's limit $H.f < 5 \times 10^9$ A m^{-1} s^{-1}, a limit at which an unwanted nonselective heating of both cancerous as well as healthy tissue may occur, as suggested by Hergt.

4. Conclusion

In conclusion, various PVPylated divalent metal-doped MFe_2O_4 (M = Ni, Co, Zn, Mg, and Sn) with noticeable aqueous stability, small sizes, high magnetization, and excellent heating efficiencies were constructed using KHB methodology. The magneto-thermal capabilities of the doped MNPs were systematically investigated under clinically-safe AMF ($f = 332.8$ kHz and $H = 170$ Oe). It was found that PVP-Ni-Fe_2O_4 and PVP-Co-Fe_2O_4 ferrite NPs displayed the highest magnetization (M_s = 80.74 and 66.17 emu g^{-1}) and heating efficiencies (SAR = 54.71 W g^{-1} and 30.57 W g^{-1}), respectively. Hyperthermia temperatures of 42 °C can be reached very fast in only ~5 min, with heating temperatures slowly increasing to reach up to 55 °C. The highest heating performance attained was as follows: PVP-$NiFe_2O_4$ > PVP-$CoFe_2O_4$ > PVP-$ZnFe_2O_4$ > PVP-$MgFe_2O_4$ > PVP-$SnFe_2O_4$, which is found to be directly correlated with their magnetic saturation. Lastly, viability assays against cancerous cells confirmed the safety profiles of the utilized PVP-ferrites. The good heating efficiencies, high SAR values, and low toxicities of the PVPylated doped MNPs, particularly Ni- and Co-doped ferrites, strongly suggest their promising potential for magneto-responsive thermal and hyperthermia applications.

Data availability

The data that supports the findings reported herein are available upon request from the corresponding author.

Author contributions

K. · H. B. conceived and designed the study. K. H. B. prepared all the samples. O. M. L. performed the characterization and magnetization of the samples. S. A. conducted the magnetic hyperthermia measurements and calculated SAR and ILP values. B. A. performed XRD and Rietveld analysis. R. A. performed MTT cell viability experiments. N. M. conducted magnetic parameters and fittings. K. H. B. analyzed the experimental data and wrote the manuscript. O. M. L. and M. H. helped with the manuscript preparation and supervision. All authors reviewed and approved the manuscript.

Conflicts of interest

The authors declare no competing financial and/or non-financial interests in relation to the work described.

Acknowledgements

This work was supported and funded by the Deanship of Scientific Research at Imam Mohammad Ibn Saud Islamic University (IMSIU) (grant number IMSIU-RP23089). The authors would like to thank the continuous support of the College of Science at University of Bahrain. Special and sincere thanks to Mrs Hawra Ahmed, Mrs Amal Alwadi, and Dr Dalaver Anjum for conducting SEM-EDX and STEM-EELS at Alba and Khalifa University of Science and Technology, respectively.

References

1 W. Wu, C. Z. Jiang and V. A. L. Roy, *Nanoscale*, 2016, **8**, 19421–19474.
2 S. Laurent, A. A. Saei, S. Behzadi, A. Panahifar and M. Mahmoudi, *Expert Opin. Drug Delivery*, 2014, **11**, 1449–1470.
3 R. A. Revia and M. Zhang, *Mater. Today*, 2016, **19**, 157–168.
4 C. S. S. R. Kumar and F. Mohammad, *Adv. Drug Delivery Rev.*, 2011, **63**, 789–808.
5 E. Kita, S. Hashimoto, T. Kayano, M. Minagawa, H. Yanagihara, M. Kishimoto, K. Yamada, T. Oda, N. Ohkohchi, T. Takagi, T. Kanamori, Y. Ikehata and I. Nagano, *J. Appl. Phys.*, 2010, **107**, 09B321.
6 Kritika and I. Roy, *Mater. Adv.*, 2022, **3**, 7425–7444.
7 G. Nandhini and M. K. Shobana, *J. Magn. Magn. Mater.*, 2022, **552**, 169236.
8 M. Johannsen, B. Thiesen, P. Wust and A. Jordan, *Int. J. Hyperthermia*, 2010, **26**, 790–795.
9 K. El-Boubbou, *Nanomedicine*, 2018, **13**, 953–971.
10 P. de la Presa, Y. Luengo, M. Multigner, R. Costo, M. P. Morales, G. Rivero and A. Hernando, *J. Phys. Chem. C*, 2012, **116**, 25602–25610.
11 O. M. Lemine, K. Omri, M. Iglesias, V. Velasco, P. Crespo, P. de la Presa, L. El Mir, H. Bouzid, A. Yousif and A. Al-Hajry, *J. Alloys Compd.*, 2014, **607**, 125–131.
12 C. Martinez-Boubeta, K. Simeonidis, A. Makridis, M. Angelakeris, O. Iglesias, P. Guardia, A. Cabot, L. Yedra,

S. Estradé, F. Peiró, Z. Saghi, P. A. Midgley, I. Conde-Leborán, D. Serantes and D. Baldomir, *Sci. Rep.*, 2013, **3**, 1652.
13 O. M. Lemine, S. Algessair, N. Madkhali, B. Al-Najar and K. El-Boubbou, *Nanomaterials*, 2023, **13**, 453.
14 J. Angadi V, N. B. Shigihalli, K. Mujasam Batoo, S. Hussain, E. Vijaya Sekhar, S. Wang and S. P. Kubrin, *J. Magn. Magn. Mater.*, 2022, **564**, 170088.
15 M. N. Kiani, M. S. Butt, I. H. Gul, M. Saleem, M. Irfan, A. H. Baluch, M. A. Akram and M. A. Raza, *ACS Omega*, 2023, **8**, 3755–3761.
16 H. Du, O. U. Akakuru, C. Yao, F. Yang and A. Wu, *Transl. Oncol.*, 2022, **15**, 101264.
17 J. Smit and H. P. J. Wijn, in *Advances in Electronics and Electron Physics*, ed. L. Marton, Academic Press, 1954, vol. 6, pp. 69–136.
18 A. Aldaoud, O. M. Lemine, N. Ihzaz, L. El Mir, S. A. Alrub and K. El-Boubbou, *Phys. B*, 2022, **639**, 413993.
19 O. M. Lemine, K. El-Boubbou, I. Orue, J. Ángel García, M. Elansary, R. Ali, L. El Mir and M. Henini, *J. Magn. Magn. Mater.*, 2023, **587**, 171279.
20 A. Kumar, N. Yadav, D. S. Rana, P. Kumar, M. Arora and R. P. Pant, *J. Magn. Magn. Mater.*, 2015, **394**, 379–384.
21 I. Sharifi, H. Shokrollahi and S. Amiri, *J. Magn. Magn. Mater.*, 2012, **324**, 903–915.
22 K. P. Hazarika and J. P. Borah, *J. Magn. Magn. Mater.*, 2022, **560**, 169597.
23 A. Manohar, V. Vijayakanth, S. V. P. Vattikuti and K. H. Kim, *Mater. Chem. Phys.*, 2022, **286**, 126117.
24 A. Manohar, V. Vijayakanth, S. V. P. Vattikuti and K. H. Kim, *Mater. Chem. Phys.*, 2022, **286**, 126117.
25 Z. Zi, Y. Sun, X. Zhu, Z. Yang, J. Dai and W. Song, *J. Magn. Magn. Mater.*, 2009, **321**, 1251–1255.
26 A. Manohar, D. D. Geleta, C. Krishnamoorthi and J. Lee, *Ceram. Int.*, 2020, **46**, 28035–28041.
27 O. M. Lemine, N. Madkhali, M. Hjiri, N. A. All and M. S. Aida, *Ceram. Int.*, 2020, **46**, 28821–28827.
28 Y. Iqbal, H. Bae, I. Rhee and S. Hong, *J. Korean Phys. Soc.*, 2016, **68**, 587–592.
29 P. V. Ramana, K. S. Rao, K. R. Kumar, G. Kapusetti, M. Choppadandi, J. N. Kiran and K. H. Rao, *Mater. Chem. Phys.*, 2021, **266**, 124546.
30 O. Oulhakem, I. Guetni, M. Elansary, M. Belaiche, Y. Mouhib, C. A. Ferdi, K. B. Alaoui and O. M. Lemine, *J. Magn. Magn. Mater.*, 2023, **587**, 171290.
31 T. Tatarchuk, A. Shyichuk, Z. Sojka, J. Gryboś, M. Naushad, V. Kotsyubynsky, M. Kowalska, S. Kwiatkowska-Marks and N. Danyliuk, *J. Mol. Liq.*, 2021, **328**, 115375.
32 A. Manohar, V. Vijayakanth, M. R. Pallavolu and K. H. Kim, *J. Alloys Compd.*, 2021, **879**, 160515.
33 K. El-Boubbou, O. M. Lemine, R. Ali, S. M. Huwaizi, S. Al-Humaid and A. AlKushi, *New J. Chem.*, 2022, **46**, 5489–5504.
34 M. Vassallo, D. Martella, G. Barrera, F. Celegato, M. Coïsson, R. Ferrero, E. S. Olivetti, A. Troia, H. Sözeri, C. Parmeggiani, D. S. Wiersma, P. Tiberto and A. Manzin, *ACS Omega*, 2023, **8**, 2143–2154.
35 R. Ghosh, L. Pradhan, Y. P. Devi, S. S. Meena, R. Tewari, A. Kumar, S. Sharma, N. S. Gajbhiye, R. K. Vatsa, B. N. Pandey and R. S. Ningthoujam, *J. Mater. Chem.*, 2011, **21**, 13388–13398.
36 Z. Ashikbayeva, D. Tosi, D. Balmassov, E. Schena, P. Saccomandi and V. Inglezakis, *Nanomaterials*, 2019, **9**, 1195.
37 M. Jamir, R. Islam, L. M. Pandey and J. P. Borah, *J. Alloys Compd.*, 2021, **854**, 157248.
38 B. Aslibeiki, N. Eskandarzadeh, H. Jalili, A. Ghotbi Varzaneh, P. Kameli, I. Orue, V. Chernenko, A. Hajalilou, L. P. Ferreira and M. M. Cruz, *Ceram. Int.*, 2022, **48**, 27995–28005.
39 A. Soufi, H. Hajjaoui, R. Elmoubarki, M. Abdennouri, S. Qourzal and N. Barka, *Appl. Surf. Sci. Adv.*, 2021, **6**, 100145.
40 S. J. Salih and W. M. Mahmood, *Heliyon*, 2023, **9**, e16601.
41 L. Zeng, W. Ren, J. Zheng, P. Cui and A. Wu, *Phys. Chem. Chem. Phys.*, 2012, **14**, 2631–2636.
42 P. Lavanya Rathi and S. Deepa, *Ceram. Int.*, 2020, **46**, 2969–2978.
43 C. Himcinschi, I. Vrejoiu, G. Salvan, M. Fronk, A. Talkenberger, D. R. T. Zahn, D. Rafaja and J. Kortus, *J. Appl. Phys.*, 2013, **113**, 084101.
44 M. S. Al Maashani, K. A. Khalaf, A. M. Gismelseed and I. A. Al-Omari, *J. Alloys Compd.*, 2020, **817**, 152786.
45 L. R. P and D. Seetharaman, *Open Ceram.*, 2022, **9**, 100222.
46 Z. M. Abdulhamid, A. A. Dabbawala, T. Delclos, R. Straubinger, M. Rueping, K. Polychronopoulou and D. H. Anjum, *Sci. Rep.*, 2023, **13**, 19705.
47 V. A. Dhumale, R. K. Gangwar, S. S. Datar and R. B. Sharma, *Mater. Express*, 2012, **2**, 311–318.
48 R. K. Gangwar, V. A. Dhumale, D. Kumari, U. T. Nakate, S. W. Gosavi, R. B. Sharma, S. N. Kale and S. Datar, *Mater. Sci. Eng., C*, 2012, **32**, 2659–2663.
49 S. Xuan, F. Wang, Y.-X. J. Wang, J. C. Yu and K. C.-F. Leung, *J. Mater. Chem.*, 2010, **20**, 5086–5094.
50 B. B. V. S. Vara Prasad, K. V. Ramesh and A. Srinivas, *J. Supercond. Novel Magn.*, 2017, **30**, 3523–3535.
51 K. Maaz, A. Mumtaz, S. K. Hasanain and A. Ceylan, *J. Magn. Magn. Mater.*, 2007, **308**, 289–295.
52 S. Talebniya, I. Sharifi, M. R. Saeri and A. Doostmohammadi, *J. Supercond. Novel Magn.*, 2022, **35**, 899–908.
53 M. Shanigaram, U. Kodam, J.-S. Noh and Y.-W. Nam, *J. Phys. Chem. Solids*, 2022, **171**, 111036.
54 V. Kumar, A. Rana, M. S. Yadav and R. P. Pant, *J. Magn. Magn. Mater.*, 2008, **320**, 1729–1734.
55 Y. Wang, L. Li, Y. Zhang, X. Chen, S. Fang and G. Li, *J. Phys. Chem. C*, 2017, **121**, 19467–19477.
56 S. Hunpratub, S. Phokha, P. Kidkhunthod, N. Chanlek and P. Chindaprasirt, *Results Phys.*, 2021, **24**, 104112.
57 R. Tiwari, M. De, H. S. Tewari and S. K. Ghoshal, *Results Phys.*, 2020, **16**, 102916.
58 B. H. Kim, N. Lee, H. Kim, K. An, Y. I. Park, Y. Choi, K. Shin, Y. Lee, S. G. Kwon, H. B. Na, J.-G. Park, T.-Y. Ahn, Y.-W. Kim, W. K. Moon, S. H. Choi and T. Hyeon, *J. Am. Chem. Soc.*, 2011, **133**, 12624–12631.
59 F. Hu, K. W. MacRenaris, E. A. Waters, T. Liang, E. A. Schultz-Sikma, A. L. Eckermann and T. J. Meade, *J. Phys. Chem. C*, 2009, **113**, 20855–20860.

60 J.-H. Park, G. von Maltzahn, L. Zhang, M. P. Schwartz, E. Ruoslahti, S. N. Bhatia and M. J. Sailor, *Adv. Mater.*, 2008, **20**, 1630–1635.
61 M. Amiri, M. Salavati-Niasari, A. Pardakhty, M. Ahmadi and A. Akbari, *Mater. Sci. Eng., C*, 2017, **76**, 1085–1093.
62 E. C. Stoner and E. P. Wohlfarth, *IEEE Trans. Magn.*, 1991, **27**, 3475–3518.
63 W. F. Brown, *Phys. Rev.*, 1940, **58**, 736–743.
64 T. E. Torres, E. Lima, M. P. Calatayud, B. Sanz, A. Ibarra, R. Fernández-Pacheco, A. Mayoral, C. Marquina, M. R. Ibarra and G. F. Goya, *Sci. Rep.*, 2019, **9**, 3992.
65 H. Fatima, T. Charinpanitkul and K.-S. Kim, *Nanomaterials*, 2021, **11**, 1203.
66 J.-P. Fortin, C. Wilhelm, J. Servais, C. Ménager, J.-C. Bacri and F. Gazeau, *J. Am. Chem. Soc.*, 2007, **129**, 2628–2635.
67 R. Hergt and S. Dutz, *J. Magn. Magn. Mater.*, 2007, **311**, 187–192.
68 R. Hergt, W. Andra, C. G. d'Ambly, I. Hilger, W. A. Kaiser, U. Richter and H. G. Schmidt, *IEEE Trans. Magn.*, 1998, **34**, 3745–3754.
69 M. Virumbrales-del Olmo, A. Delgado-Cabello, A. Andrada-Chacón, J. Sánchez-Benítez, E. Urones-Garrote, V. Blanco-Gutiérrez, M. J. Torralvo and R. Sáez-Puche, *Phys. Chem. Chem. Phys.*, 2017, **19**, 8363–8372.
70 M. Kallumadil, M. Tada, T. Nakagawa, M. Abe, P. Southern and Q. A. Pankhurst, *J. Magn. Magn. Mater.*, 2009, **321**, 1509–1513.
71 R. Ali, N. Samman, H. Al Zahrani, A. Nehdi, S. Rahman, A. L. Khan, M. Al Balwi, L. A. Alriyees, M. Alzaid, A. Al Askar and M. Boudjelal, *BMC Cancer*, 2017, **17**, 803.